15. A. A. Amsden, H. M. Ruppel, C. W. Hirt, "SALE: A Simplified ALE Computer Program for Fluid Flow at All Speeds" (Report LA-8095, Los Alamos National Laboratory, Los Alamos, NM, 1980).
16. H. J. Melosh, E. A. Ryan, E. Asphaug, *J. Geophys. Res.* **97**, 14735 (1992).
17. J. N. Head, *Eos* **76**, F336 (1995).
18. H. J. Melosh, *Icarus* **59**, 234 (1984).
19. The most common impact angle is 45°, which constitutes an inherently 3D problem that is computationally very expensive. In oblique impacts, the shock wave is stronger down-range and weaker up-range. However, it is still hemispherical and will still weaken as $1/r^2$. Moreover, the propagation of the shock wave will still be affected by the physical nature of the medium (damaged versus undamaged). The azimuthal dependence of shock wave strength might modulate the number of ejected fragments from a crater of a given size, but it should not change our finding that the presence of an impact-generated regolith suppresses spall velocity and hence biases the ejecta launched from Mars in favor of young material.
20. W. F. Bottke Jr., M. C. Nolan, R. Greenberg, R. A. Kolvoord, in *Hazards Due to Comets and Asteroids*, T. Gehrels, Ed. (Univ. of Arizona Press, Tucson, AZ, 1994), pp. 337–357.
21. H. J. Melosh, *Impact Cratering: A Geologic Process* (Oxford Univ. Press, New York, 1989).
22. J. von Neuman, J. D. Richtmyer, *J. Appl. Phys.* **21**, 232 (1950).
23. J. N. Head, H. J. Melosh, *31st Lunar Planet. Sci. Conf.*, abstract 1937 (2000).
24. R. M. Schmidt, K. R. Housen, *Int. J. Impact Eng.* **5**, 543 (1987).
25. K. L. Tanaka, D. H. Scott, R. Greeley, in *Mars*, H. H. Kieffer, B. M. Jakosky, C. W. Snyder, M. S. Matthews, Eds. (Univ. of Arizona Press, Tucson, AZ, 1992), pp. 345–382.
26. In contrast, assume that only 10^6 fragments must be launched from Mars to expect to have one in our meteorite collection and that these fragments derive from a parent fragment undergoing an in-space breakup event. One million 20-cm-diameter stones have a total volume of ~4200 m^3. This is equivalent to a single parent fragment 20 m across. Such a large fragment would have to come from a much larger and therefore much rarer impact than the ones modeled here. Consider further that to create a large number of different CRE ages, this fragment must undergo multiple breakup events, or a group of such mother fragments must each undergo breakup events at different times. Moreover, consider a 10-m-radius ejecta fragment as the parent of eight Shergottites. If the cosmic ray shielding depth is 2 m, then about half the volume of the fragment is shielded and will not present a 2-π exposure history. A random draw of eight stones from the entire fragment would then have a $(1/2)^8$ or 1/256 chance of all stones presenting a single-stage CRE history. Because multiple ages are required, and at each step the ratio of two-stage to single-stage CRE history material increases, the odds for recovering only 4-π exposed stones drops even more. Finally, an impact that launches a 20-m-diameter fragment will likely launch an enormous number of decimeter-scale fragments, which would be more likely to reach Earth than would pieces of the 20-m fragment (*28*).
27. The data in Fig. 3 show that a low-velocity regolith layer may be irrelevant with regard to launching lunar meteorites because of the much lower lunar escape velocity of ~2.3 km/s. At this value, the spall velocity is the same in our models regardless of the presence of a regolith layer. The launch efficiency is then the same whether the surface is pristine or a deep regolith. Hence, the mechanism by which the launch of martian meteorites is biased in favor of young material cannot operate on the Moon. One implication of this is that lunar meteorite petrology should be representative of the observed surface units. This appears to be the case (*9*). The delivery time scale is much less than for martian meteorites, and the maximum terrestrial age is evidently ~0.1 Ma. This implies that meteorites found on Earth are predominately from the most recent lunar impacts, because samples from older impacts would have been destroyed long ago by the terrestrial environment. As a test of our model, we simulated lunar meteorite launch, modeling the lunar surface as basaltic covered by a regolith of the same material, but damaged. We found that the expected number of source craters is consistent with that estimated from the lunar meteorites in hand, but only for impacts that are recent compared to the Moon-to-Earth delivery time scale. Samples from older impacts appear to be greatly underrepresented in the meteorite collection with regard to our model results. The few lunar meteorites with launch ages greater than a few hundred thousand years (up to ~10 Ma) are found only if they have been sequestered in the relatively benign space environment for most of their post-launch history (*29*).
28. G. W. Wetherill, *Meteoritics* **19**, 1 (1984).
29. J. N. Head, *32nd Lunar Planet. Sci. Conf.*, abstract 1768 (2001).
30. R. Score, M. M. Lindstrom, *Antarct. Meteorite Newsl.* **13** (1990).
31. C. Satterwhite, B. Mason, *Antarct. Meteorite Newsl.* **14** (1991).
32. R. Score, B. Mason, *Antarct. Meteorite Newsl.* **18** (1995).
33. H. Kojima, M. Miyamoto, P. H. Warren, *Antarct. Meteorite Res.* **10**, 3 (1997).
34. J. N. Grossman, *Meteorit. Planet. Sci.* **34**, A169 (1995).
35. K. Nagao, T. Nakamura, Y. N. Miura, N. Takaoka, *Antarct. Meteorite Res.* **10**, 125 (1997).
36. E. O. Jagoutz, O. Bodganovski, N. Krestina, R. Jotter, *30th Lunar Planet Sci. Conf.*, abstract 1808 (1999).
37. F. Langenhorst, A. Greshake, *Meteorit. Planet. Sci.* **34**, 43 (1999).
38. M. Eugster, A. Weigel, E. Polnau, *Geochem. Cosmochim. Acta* **61**, 2749 (1997).
39. L. Folco, I. A. Franchi, P. Scherer, L. Schultz, C. T. Fillinger, *Meteorit. Planet. Sci.* **34**, A36 (1999).
40. K. Nishiizumi *et al.*, *30th Lunar Planet Sci. Conf.*, abstract 1966 (1999).
41. The authors acknowledge helpful reviews, which improved the quality of this paper.

19 August 2002; accepted 24 October 2002
Published online 7 November 2002;
10.1126/science.1077483
Include this information when citing this paper.

REPORTS

Formation of Giant Planets by Fragmentation of Protoplanetary Disks

Lucio Mayer,[1*†] Thomas Quinn,[1*] James Wadsley,[2] Joachim Stadel[3†]

The evolution of gravitationally unstable protoplanetary gaseous disks has been studied with the use of three-dimensional smoothed particle hydrodynamics simulations with unprecedented resolution. We have considered disks with initial masses and temperature profiles consistent with those inferred for the protosolar nebula and for other protoplanetary disks. We show that long-lasting, self-gravitating protoplanets arise after a few disk orbital periods if cooling is efficient enough to maintain the temperature close to 50 K. The resulting bodies have masses and orbital eccentricities similar to those of detected extrasolar planets.

About 100 extrasolar planets have been detected by the wobble they induce on their star (*1*, *2*). Their masses range from about one Jupiter mass (M_J) to more than 10 M_J and have orbits ranging from nearly circular to very eccentric. In the standard core-accretion model, giant planets might require longer than 10^6 years to form (*3*, *4*), which could exceed observed disk lifetimes (*5*–*7*). In particular, more than 80% of the stars in the Galaxy probably formed in dense clusters like those in the Orion nebula (*8*) where the ultraviolet radiation of bright stars can ablate the gaseous disk in far less than a million years (*5*, *6*). Hence giant planet formation must occur quickly, or such planets would be rare. Even in the case where a large solid core is assembled rapidly enough, torques acting between the disk and the protoplanets are believed to induce its complete inward migration in a few thousand years (*9*, *10*). Planets could therefore sink toward the star before being able to accrete the large gaseous masses observed (*11*, *12*). Alternatively, giant planets could coagulate directly in the gas component as a result of gravitational instabilities in a cold disk with a mass comparable to that adopted in the core-accretion model (*13*, *14*). Simulations done with codes that solve the hydrodynamical equations on a fixed grid show that slightly perturbed disks form strong spiral arms and overdensities at $R > 10$ astronomical units (AU) (*15*, *16*) where the temperature can be lower than 60 K (*17*, *18*). The trigger of the instability might come from material of the protostellar cloud infalling onto the disk (*13*). If these condensations are long-lasting and can contract to planetary densities, gravitational instability would be the prevailing formation mechanism for giant planets because it takes less than a thousand years (*13*, *15*). Solid cores with masses as low as currently estimated for Jupiter [between 0 and 10 Earth masses (*19*)] could then form inside the gaseous protoplanets due to dust and planetesimals driven there by local pressure gradients in a few thousand years (*20*).

However, due to the limitations of the techniques, simulations have not yet been able to show convincingly that the overdensities are not sheared apart by the tidal field of the star, nor that they can collapse into protoplanets (*16*). One needs to achieve a high spatial resolution for such a purpose. Smoothed particle hydrodynamics (SPH) simulations (*21*) describe the gaseous medium as a collection of particles and can follow very high densities. Disks have been simulated with this technique in the past but with fewer than 10^5 particles (*22–24*); with such a low-mass resolution, the evolution of the density distribution is considerably noisy and artificial fragmentation can take place (*23*).

Here we report on the results of three-dimensional (3D) SPH simulations of marginally unstable disks of molecular hydrogen using as many as 1 million particles. The disks extend from 4 to 20 AU initially, and they are in nearly keplerian rotation around a solar mass star represented by a point mass. They have a minimum Toomre Q parameter, Q_{min}, of either 1.4 or 1.75, and masses of 0.1 and 0.08 mass of the sun ($M_\odot$), respectively (Fig. 1). In the initial stage, the disks are evolved with the use of a locally isothermal equation of state; the initial temperature decreases with radius following a power law profile predicted by detailed calculations of thermal balance between the central star, the disk, and the protostellar cloud (*17*) and is then held fixed locally. This approximation is based on the assumption that the cooling time is so short that the disk radiates away any thermal energy injection on a time scale shorter than the orbital time. This seems to be supported by recent grid-based simulations that include radiative transfer in the diffusion approximation (*16*) but neglect the irreversible heating which can be generated by shock waves in a strongly unstable disk (*25*, *26*). Although further investigation on the balance between heating and cooling in realistic disks will be needed in the future (*26*), here we concentrate on showing that actual protoplanets can form if the disk remains cold for long enough (*27*).

After ~150 years, corresponding to about five orbital periods at a radius of 10 AU, the disks develop trailing spiral arms and local overdensities at $R > 10$ AU. In the lighter disk, the spiral arms grow in amplitude up to about 300 years, and then they settle down to a nearly stationary pattern (Fig. 1). In the more massive disk ($Q_{min} = 1.4$), a two-armed mode grows in amplitude up to the point where, after about 200 years, fragmentation occurs along the arms, and more than one distinct clump appears (Fig. 1); then additional strong arms appear even at $R \gtrsim 7$ to 8 AU, and more clumps are formed. Inside this radius, the disk is too hot for condensations to form. Clumps quickly contract, reaching central densities of more than 10^5 times the local density in a matter of a few orbital periods (tens of years). These condensations are self-gravitating, their masses being larger than the local Jeans mass (*28*), and they easily resist stellar tides.

Such dense objects would be optically thick and would be unable to cool radiatively as efficiently as assumed by the locally isothermal approximation (*16*, *25*). Therefore, we ran again the same initial conditions, changing the equation of state to adiabatic (*29*) as soon as the spiral modes approached fragmentation, namely when they reached a density around 10 times higher than the initial local density (*16*, *26*). The equation of state is changed throughout the disk. After 350 years, nonaxisymmetric features in the disk are weaker compared with the isothermal simulation, yet clump formation has proceeded. Nearly as many clumps as in the locally isothermal run are still present at $R > 10$ AU and have central densities 10^5 times higher than the local density. The clumps are rapidly rotating spheroids; assuming conservation of angular momentum, bodies of about 1 M_J would have a rotation period of a few hours if they were allowed to contract further and reach the density of Jupiter.

The masses of the clumps, shortly after all of them are in place (after ~350 years), ranged from 1 to 5 M_J (all gas at densities at least 10 times higher than the initial local density is identified as a clump), comparable to the masses of extrasolar planets (*1*). Clumps formed along the same spiral arm collide and merge into a more massive object, sooner or later. Time steps can be as small as a few hours inside the clumps, which slows down the simulation considerably. To keep following the clumps on a longer time scale, we resorted to simulations with a resolution five times lower. By 350 years, seven clumps with masses comparable to the largest among the 13 clumps present in the

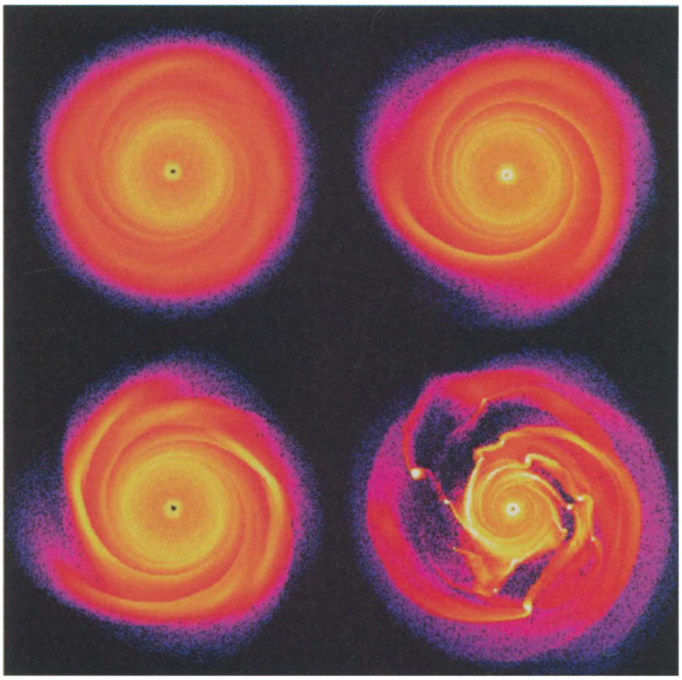

Fig. 1. Snapshots of the simulations showing the protoplanetary disks seen face-on at different times. The color-coded density on a logarithmic scale is shown to 20 AU. Brighter colors trace higher densities (starting with white and going to dark blue through yellow, red, and magenta), and the density ranges between 10^{-14} and 10^{-6} g/cm^3. The evolution of two disks with a different initial minimum Toomre Q parameter, Q_{min}, is shown. The Toomre parameter at a given disk location is defined as $Q = \Omega v_s / \pi G \Sigma$, where Σ is the gas surface density, Ω is the angular velocity, G is the gravitational constant, and v_s is the sound speed ($v_s = \sqrt{P/\rho}$, where P is the pressure and ρ is the density of the gas). Disks have a surface density profile $\Sigma \sim r^{-3/2}$ (*12*) and temperature profiles as in the Boss model (*15–17*). Q reaches its minimum at $R > 10$ AU, where the temperature is as low as 50 K, whereas $Q > 4$ close to the inner disk boundary, where the temperature is around 650 K. The two upper panels show the disk with initial $Q_{min} \sim 1.75$ ($M_{disk} = 0.08\ M_\odot$) at $T = 160$ years (left) and $T = 350$ years (right), whereas the two lower panels show the disk with $Q_{min} \sim 1.4$ ($M_{disk} = 0.1\ M_\odot$) at $T = 160$ years and $T = 350$ years. Gravity is softened on scales of 0.06 AU for disk particles. The central stellar potential is exactly keplerian at 2.5 AU, and it is softened on smaller scales to speed the computation. Both the central star and the inner disk boundary are free to move. The simulations were performed with GASOLINE, a parallel N-body/SPH code in which gravity is computed using a binary tree (*34*).

[1]Department of Astronomy, University of Washington, Seattle, WA 98195, USA. [2]Department of Physics & Astronomy, McMaster University, 1280 Main St. West, Hamilton, ON L8S 4M1, Canada. [3]University of Victoria, Department of Physics and Astronomy, 3800 Finnerty Road, Elliot Building, Victoria, BC V8W 3PG, Canada.

*To whom correspondence should be addressed. E-mail: lucio@physik.unizh.ch, trq@astro.washington.edu

†Present address: Institute of Theoretical Physics, University of Zurich, Winterthurerstrasse 190, CH-8057 Zurich, Switzerland.

higher resolution simulation had formed and were then followed for about 1000 years. We ran both a locally isothermal and an adiabatic simulation to determine the role of the thermal structure of the disk in shaping the dynamics of clumps.

Clumps are born on orbits with a wide range of eccentricities driven by the underlying strongly nonaxisymmetric disk potential. These orbits then evolve in a variety of ways (Fig. 2). The smoother disk in the adiabatic run leads to less eccentric orbits; also, the higher pressure of the gas reduces considerably gas accretion by clumps. Slightly more circular orbits reduce the rate of close encounters and mergers between clumps relative to the isothermal run. After nearly 1000 years, three clumps were left in the adiabatic run (Fig. 2) as opposed to two clumps in the isothermal run. These numbers are comparable to those of extrasolar giant planets in multiple systems (*1*). The masses of the surviving clumps, located between 3 and 20 AU, were in the range 2 to 6 M_J in the adiabatic case and twice as big in the isothermal case. Most of the clumps have orbits with final eccentricities between 0.1 and 0.3 (Fig. 2), like many of the observed extrasolar planets (Fig. 2). The simulated protoplanets enter a rather quiescent evolutionary phase (no more mergers occur) several orbital periods before the end of the simulations. However, inward migration might continue on time scales longer than those explored here (*10–12*), and orbits can also change due to interactions between the planets (*30*).

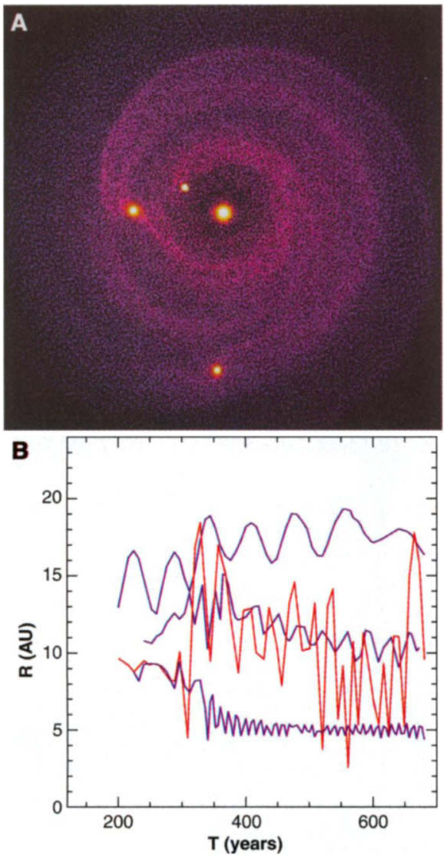

Fig. 2. Late stage of disk evolution. (**A**) A face-on view of the disk after 800 years for the 200,000 particles simulation in which the equation of state is switched to adiabatic after about 200 years. The color-coded logarithmic density (Fig. 1) is plotted out to 25 AU. (**B**) Three giant protoplanets are left, and their orbital evolution (blue lines) is shown, together with that of a clump from the simulation where the equation of state is kept isothermal (red line). Each of the remaining clumps is the end result of a series of mergers. We follow the orbital evolution of the most massive progenitor. The complex combination of torquing by the nonaxisymmetric disk and interactions with other clumps changes the orbital eccentricity and mean radius of the orbits. Overall the orbital evolution is considerably more complex than the nearly steady inward migration expected in light, axisymmetric disks, eventually halting once the planet has cleared a gap (*9–12*).

This work shows that gravitational instability can actually form self-gravitating protoplanets and that long-lived systems with masses and orbits consistent with those of extrasolar planets arise. All this requires is to start with a marginally unstable disk ($Q_{min} = 1.4-1.5$) in which radiative cooling is efficient during the initial growth of the overdensities. We tested whether hotter disks starting from a considerably higher Q_{min} (~ 2) can also become strongly unstable and form clumps if they are slowly cooled to temperatures comparable to those used in the disks starting with $Q_{min} \sim 1.4$ (*31*). Therefore, clump formation does not depend on how the disk reaches the state used in our initial conditions. Ice giant planets, like Uranus and Neptune, might also be formed by the same mechanism after a strong ultraviolet flux from nearby bright stars has photoionized the envelopes of protoplanets more massive than Jupiter, leaving a mostly metallic core (*20*). Because instabilities occur quickly, future observations of planets around very young stars will be a test for this model. In addition, direct imaging of giant planets at large distances ($R > 50$ AU) from the stars (*32*) could also provide support to this model, because the outermost regions of the disk would be even cooler (and surface density and angular velocity fall equally with radius, i.e., $r^{-3/2}$), Q will be still decreasing at $R > 20$ AU, and thus fragmentation should occur out to these large distances. On the contrary, Jupiter-like planets would not form at such large distances in the core-accretion model because coagulation of planetesimals into a solid core would take too long with the small surface densities involved (*33*). Future observations of the gaseous medium in disks at different evolutionary stages, for example with the Space Infrared Telescope Facility (SIRTF), will help constrain the evolution of disk structure and show whether it is consistent with the gravitational instability picture.

References and Notes

1. G. W. Marcy, R. P. Butler, *Publ. Astron. Soc. Pac.* **112**, 137 (2000).
2. ———, *Annu. Rev. Astron. Astrophys.* **36**, 57 (1998).
3. J. B. Pollack *et al.*, *Icarus* **124**, 62 (1996).
4. J. Lissauer, *Nature* **409**, 23 (2001).
5. J. Bally, L. Testi, A. Sargent, J. Carlstrom, *Astron. J.* **116**, 854 (1998).
6. C. Briceno *et al.*, *Science* **291**, 93 (2001).
7. K. E. Haisch Jr., E. A. Lada, C. J. Lada, *Astrophys. J.* **553**, L153 (2001).
8. H. B. Throop, J. Bally, J. L. W. Esposito, M. J. McCaughrean, *Science* **292**, 1686 (2001).
9. D. N. C. Lin, J. C. B. Papaloizou, *Astrophys. J.* **309**, 846 (1986).
10. G. Bryden, X. Chen, D. N. C. Lin, R. P. Nelson, J. C. B. Papaloizou, *Astrophys. J.* **514**, 344 (1999).
11. R. P. Nelson, J. C. B. Papaloizou, F. Masset, W. Kley, *Mon. Not. R. Astron. Soc.* **318**, 18 (2000).
12. H. Tanaka, T. Takeuchi, W. Ward, *Astrophys. J.* **565**, 1257 (2002).
13. A. P. Boss, *Astrophys. J.* **503**, 923 (1998).
14. S. J. Weidenschilling, *Astrophys. Space. Sci.* **51**, 153, (1977).
15. A. P. Boss, *Science* **276**, 1836 (1997).
16. ———, *Astrophys. J.* **563**, 367 (2001).
17. ———, *Annu. Rev. Astron. Astrophys.* **26**, 53 (1998).
18. P. D'Alessio, N. Calvet, L. Hartmann, *Astrophys. J.* **553**, 321 (2001).
19. T. Guillot, *Science* **286**, 72 (1999).
20. A. P. Boss, G. W. Wetherill, N. Haghighipour, *Icarus* **156**, 291 (2002).
21. R. A. Gingold, J. J. Monaghan, *Mon. Not. R. Astron. Soc.* **181**, 357 (1977).
22. G. Laughlin, P. Bodenheimer, *Astrophys. J.* **436**, 335 (1994).
23. A. F. Nelson, W. Benz, F. C. Adams, D. Arnett, *Astrophys. J.* **502**, 342 (1998).
24. A. F. Nelson, W. Benz, T. V. Ruzmaikina, *Astrophys. J.* **529**, 457 (2000).
25. B. K. Pickett, P. Cassen, R. H. Durisen, R. Link, *Astrophys. J.* **529**, 1034 (2000).
26. B. K. Pickett, R. H. Durisen, P. Cassen, C. Mejia, *Astrophys. J.* **540**, L95 (2000).
27. Artificial viscosity is used in both the momentum and the energy equation, but its contribution is minimized when the local flow is purely shearing by means of a correction term originally introduced by D. S. Balsara [*Comput. Phys.* **121**, 357 (1995)]; the latter term is necessary to prevent SPH from generating a large artificial viscosity in a purely shearing flow. In addition, when the disk evolves following a locally isothermal equation of state, any entropy generated by the viscosity term is assumed to be instantly radiated away.
28. The Jeans mass is always resolved by more than several thousand particles at the locations of the clumps; this resolution is more than an order of magnitude higher than required to avoid artificial fragmentation based on the criteria developed by M. Bate and A. Burkert [*Mon. Not. R. Astron. Soc.* **288**, 1060 (1997)] for 3D SPH simulations.
29. In this regime, reversible heating arising from compressions is not radiated away, and the artificial viscosity creates irreversible heating in regions where shock waves occur.
30. C. Terquem, J. C. B. Papaloizou, *Mon. Not. R. Astron. Soc.* **332**, L39 (2002).
31. For this test, we increased the temperature of the more massive disk model (resolved by 200,000 particles) by a factor of two, reaching 100 K in the outer region; 350 years after the start of the simulations, the disk was still fairly axisymmetric and we started cooling it at the constant rate of about 0.2 K/year. The disk underwent increasingly strong spiral instabilities as it was cooled down, which produced an inward flux of mass and outward flux of angular momentum, but, overall, the outer surface density barely changed. Therefore, reaching a temperature only slightly smaller than that used in the standard initial conditions (42 K as opposed to 50 K) was enough to compensate for the decrease of surface density and give rise to clump formation after about

650 years. (Cooling was stopped when fragmentation was approached.)
32. K. L. Luhman, R. Jayawardhana, *Astrophys. J.* **566**, 1132 (2002).
33. E. W. Thommes, M. J. Duncan, H. F. Levison, *Astron. J.* **123**, 2862 (2002).
34. J. Stadel, J. Wadsley, D. Richardson, in *High Performance Computing Systems and Applications*, M. J. Dimoupulos, K. F. Lie, Eds. (Kluwer Academic, Boston, 2002), p. 501.
35. The authors thank G. Laughlin, D. Hollenbach, and A. Boss for useful and stimulating discussions. Simulations were carried out at the Pittsburgh Supercomputing Center and at Consorzio Interuniversitario per il Calcolo Automatico dell'Italia Nord Orientale. This research was supported by a grant from the NSF and by the NASA Astrobiology Institute.

22 August 2002; accepted 4 November 2002

In Vivo Imaging of Quantum Dots Encapsulated in Phospholipid Micelles

Benoit Dubertret,[1,3]*† Paris Skourides,[2] David J. Norris,[3,4]* Vincent Noireaux,[1] Ali H. Brivanlou,[2] Albert Libchaber[1,3]

Fluorescent semiconductor nanocrystals (quantum dots) have the potential to revolutionize biological imaging, but their use has been limited by difficulties in obtaining nanocrystals that are biocompatible. To address this problem, we encapsulated individual nanocrystals in phospholipid block–copolymer micelles and demonstrated both in vitro and in vivo imaging. When conjugated to DNA, the nanocrystal-micelles acted as in vitro fluorescent probes to hybridize to specific complementary sequences. Moreover, when injected into *Xenopus* embryos, the nanocrystal-micelles were stable, nontoxic ($<5 \times 10^9$ nanocrystals per cell), cell autonomous, and slow to photobleach. Nanocrystal fluorescence could be followed to the tadpole stage, allowing lineage-tracing experiments in embryogenesis.

Nanometer-scale semiconductor crystallites (known as nanocrystals or quantum dots) (*1–3*) could dramatically improve the use of fluorescent markers in biological imaging (*4*, *5*). Because these colloidal particles act as robust, broadly tunable nanoemitters that can be excited by a single light source, they could provide distinct advantages over current in vitro and in vivo markers (e.g., organic dyes and fluorescent proteins). However, before nanocrystals can be widely used as biolabels, they must maintain three properties under aqueous biological conditions: efficient fluorescence, colloidal stability, and low nonspecific adsorption. Unfortunately, despite recent advances (*4–12*), these conditions have not been simultaneously satisfied, limiting the development of in vivo applications of nonaggregated (or individual) semiconductor nanocrystals.

The main challenge is that the quantum dots (QDs), as synthesized, have hydrophobic organic ligands coating their surface (*2*, *3*). To make the QDs water soluble, these organophilic surface species are generally exchanged with more-polar species, and both monolayer (*5*, *6*) and multilayer (*4*) ligand shells have been pursued. Although the monolayer method is reproducible, rapid, and produces QDs with a regular, well-oriented, thin coating, their colloidal stability is poor (*9*). In contrast, the multilayer method yields QDs that are stable in vitro (*8*), but the coating process is long and the coating is difficult to control. A more serious concern is that both approaches still produce QDs that tend to aggregate and adsorb nonspecifically. To resolve this problem, researchers have explored two additional coatings. First, the outer ligand shell of the QD has been overcoated with proteins adsorbed through hydrophobic or ionic interactions (*7*). Other layers can then be added to allow conjugation with specific biomolecules. Indeed, this method has provided new reagents for fluoroimmunoassays (*10*). Second, the outer ligand shell has been overcoated with surfactants or polymers to prevent nonspecific adsorption of biomolecules while still permitting bioconjugation. For example, silica-coated QDs have been further modified with small monomers of poly(ethylene glycol) to reduce nonspecific adsorption (*11*).

Despite these efforts, nonspecific adsorption and aggregation still occur when QDs are used in biological environments. Studies of cellular uptakes of QDs report large aggregate formation inside the cell (*5*, *13*). The same aggregation problems are reported when QDs are used for fluorescence in situ hybridization (*14*), or as markers for molecular recognition on cell surfaces (*15*, *16*). Consequently, the use of QDs in biological applications is still limited and primarily confined to in vitro studies.

We found, however, that without any surface modifications, individual ZnS-overcoated CdSe QDs (*2*, *3*) could be encapsulated (*17*) in the hydrophobic core of a micelle composed of a mixture of *n*-poly(ethylene glycol) phosphatidylethanolamine (PEG-PE) and phosphatidylcholine (PC) (Fig. 1A). PEG-PEs are micelle-forming hydrophilic polymer-grafted lipids (*18*, *19*) comparable to naturally occurring carriers such as lipoproteins and viruses (*20*). They have been used for drug delivery (*21*) and diagnostic imaging (*22*). The advantage of these micelles is that they are very regular in size, shape, and structure (*23*). In addition, their outer surface comprises a dense layer of PEG polymers that is poorly immunogenic and antigenic and acts as excellent repellent for biomolecules (*24*). Further, both the PEG content and length can be adjusted precisely.

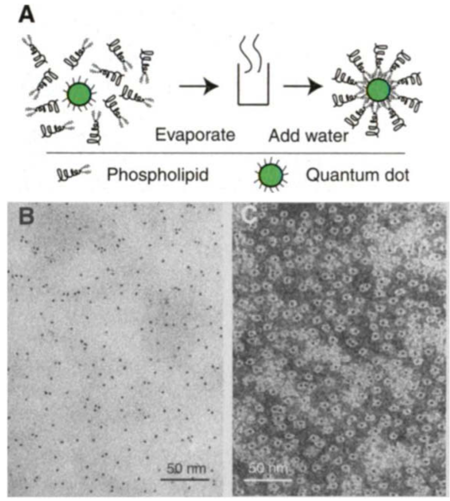

Fig. 1. QD-micelle formation and characterization. **(A)** Schematic of single-QD encapsulation in a phospholipid block–copolymer micelle. **(B)** TEM image of QD-micelles dried on a carbon-Formvar–coated 200-mesh nickel grid. Only the QDs inside the micelle core are visible. The particles appear evenly spread on the surface. Although some clusters of two to four QDs are visible, most of the QDs are isolated, suggesting that a majority of micelles contain a single QD. **(C)** TEM image of the phospholipid layer obtained by negative staining with 1% PTA (phosphotungstic acid) at pH 7. With this technique, both the QD and the micelle can be visualized at the same time. The QD (dark spot) appears surrounded by a white disk of unstained phospholipids that stands out against the stained background. A JEOL 100CX TEM was operated at 80 kV.

[1]Center for Studies in Physics and Biology, [2]Laboratory of Molecular Embryology, The Rockefeller University, 1230 York Avenue, New York, NY 10021, USA. [3]NEC Research Institute, 4 Independence Way, Princeton, NJ 08540, USA. [4]Department of Chemical Engineering and Materials Science, University of Minnesota, 421 Washington Avenue SE, Minneapolis, MN 55455, USA.

*To whom correspondence should be addressed. E-mail: benoit.dubertret@espci.fr, dnorris@umn.edu
†Present address: UPRA0005, CNRS and ESPCI, Laboratoire d'Optique Physique, 10 rue Vauquelin, 75005 Paris, France.